

Structural and optical characterization of WO₃ and WO₃/rGO nanocomposites synthesized by a simple chemical method

D.E. Ortega-Martínez, R. Agustín-Serrano, F. Caballero-Briones, F. Chalé-Lara, C. Guarneros-Aguilar

The chemical structure and morphology of inorganic metal oxides have attracted increasing interest because of these parameters directly influence their sensing properties. Additionally, the incorporation of reduced graphene oxide (rGO) favors an increase in the sensitivity of these composites. Tungsten oxide (WO₃) and tungsten oxide/reduced graphene oxide (rGO) nanocomposites with 3 wt% (WO₃/rGO) were prepared via reflux method. X-ray Diffraction (XRD), Raman Spectroscopy and Scanning Electron Microscopy (SEM) techniques were used to study the crystalline structure and morphology properties of the prepared WO₃ and WO₃/rGO nanocomposites. The diffraction pattern of WO₃ shows the diffraction peaks of tungsten trioxide hydrate (WO₃(H₂O), tungstite) with orthorhombic structure; however, with the annealing at 500 °C occur a phase transformation to the monoclinic structure. The incorporation of rGO into the WO₃ matrix did not modify its monoclinic chemical structure. The crystallite size of the reduced composites increases as the percentage of rGO increases. Furthermore, the optical properties of WO₃/rGO nanocomposites were characterized by Ultraviolet-Visible Diffuse Reflectance Spectroscopy (UV-Vis DRS). The band gap of WO₃/rGO composites varies between 3.32 and 3.35 eV. SEM images of WO₃ show structures of nanoplates with rectangular transversal section.

Introduction



Tungsten trioxide (WO₃) it is a n-type transition metal oxide semiconductor with band gap from 2.6 to 3.0 eV and different crystal phases which are formed following the sequence; monoclinic II (ε-WO₃, < 230 K), triclinic (δ-WO₃, 230 – 290 K), monoclinic I (γ-WO₃, 290 – 603 K), orthorhombic (β-WO₃, 603 – 1013 K), and tetragonal (α-WO₃, > 1013 K). However, monoclinic I is the most stable phase at room temperature [1]. According to the applications, electrochromic, sensing, photocatalytic, photo imaging systems and solar energy collectors or thermoelectric, it can be obtained in bulk or in thin film form; however, the structural, morphological, and electric properties depend on the synthesis method.


Some methods for the WO₃ synthesis are hydrothermal [2,3], Pechini [4], chemical bath [5], chemical vapor deposition [6], sol-gel [7], spray pyrolysis [8], electrodeposition [9], thermal oxidation [10], and sputtering [11]. Reflux is a simple technique, with high yield and easy operation commonly used in organic chemical synthesis in which chemical reactions occur at the solvent boiling temperature; the energy necessary for the reaction is obtained by heating the reaction solution over long periods of time, under atmospheric pressure and at constant volume. The control of these parameters provides benefits in the phase and morphology of the nanostructures [12]. This technique has been used for the synthesis of carbon nanotubes (CNTs) compounds at different contents of novel hexagonal tungsten oxide (h-WO₃) nanoflakes. On this paper, the nanocomposites were prepared via a one-step hydrothermal method, obtaining a crystal structure and morphology of WO₃ without change with the incorporation of CNTs, but caused abnormal decrease of the sample's surface area [13].


WO₃ has been synthesized by hydrothermal methods using sodium tungstate dihydrate (Na₂WO₄·2H₂O) and nitric acid (HNO₃). First, refluxed in HNO₃ solution for 12 hours at 120 °C. After cooling down to room temperature, the refluxed CNT's suspension was added. The suspension was then transferred into a stainless-steel autoclave for

24 hours. Powder sample was obtained after cleaning the hydrothermal product with distilled water [13].

On the other hand, graphene has been attractive due to its high Young's modulus of 1.0 TPa, intrinsic stress of 130 ± 10 GPa, third order elastic stiffness (-2.0 TPa) [14], and high specific surface area (1315 m²/g, theoretical value for one side of a graphene sheet) [15]. Also, its high thermal conductivity (4.8 – 5.3 × 10³ W/mK) [16], high carrier mobility (even up to 10⁵ cm²/Vs at 300 K), ballistic transport, linear current-voltage characteristic, huge sustainable currents (> 10⁸ A/cm²) [17,18], and high transparence in visible spectra (90%). The combination of these properties with other materials properties such as polymer, metal, and semiconductor, can improve the functionality of different electronic and optical devices. However, for most applications, it's important that the graphene build chemical bonds, otherwise, free-standing graphene is not mechanically stable and tends to roll up. The incorporation of rGO into WO₃/rGO composites brings significant improvements in the electrochemical, structural and practical

D. E. Ortega-Martínez , F. Chalé-Lara 
 Instituto Politécnico Nacional, CICATA
 Altamira, Tamps. 89600, México.

Ricardo Agustín-Serrano 
 Benemérita Universidad Autónoma de Puebla, Facultad de
 Ciencias Físico-Matemáticas, Puebla, Pue. 72520, México.

Felipe Caballero-Briones 
 Instituto Politécnico Nacional, Tecnologías y Materiales para
 Energía, Salud y Medio Ambiente (GESMAT), CICATA Altamira
 Altamira, Tamps. 89600, México.

C. Guarneros-Aguilar 
 CONAHCYT-Instituto Politécnico Nacional, CICATA Altamira,
 Altamira, Tamps. 89600, México.

Received: September 12th, 2024.

Accepted: February 14th, 2025.

Published: March 28th, 2025.

© 2025 by the authors. Creative Commons Attribution
https://doi.org/10.47566/2025_syv38_1-250301

properties of the material, justifying its use in specific applications. rGO provides higher electrical conductivity and a large surface area, facilitating charge transport and increasing catalytic activity, resulting in improved sensitivity and selectivity for the detection of contaminants such as 4-chlorophenol [19], and triclosan [20]. Furthermore, this combination has demonstrated a significantly lower detection limit and sharper oxidation currents compared to unmodified electrodes. Structurally, rGO restricts the growth of WO₃ crystals, generating smaller grain sizes and higher thermal and mechanical stability. In practical applications, the WO₃/rGO composite has excelled in sensors for environmental and biological sample analysis, achieving high recovery and reproducible performance in complex media such as water and soil. Furthermore, its use in electrochromic devices has demonstrated higher coloring efficiency, faster switching times, and improved cycling stability. However, while the benefits are evident, the effectiveness of rGO may depend on the synthesis method and operating conditions, suggesting the need for optimization to maximize its advantages in specific applications. Therefore, the added value of rGO in WO₃/rGO composites lies in its ability to significantly improve the functional properties of the material, positioning it as a promising solution for advanced electrochemical sensors and functional materials in emerging technologies [19-21].

Therefore, the preparation of reduced graphene oxide is required to add it to the nanocomposites and thus increase their hydrophilic character and provide a therefore been very promising for surface functionalization [22]. Although reduced graphene oxide (rGO) has lower electrical conductivity and slower carrier mobility than graphene because of the chemical functional groups attached to the carbon plane, the use of the rGO in the nanocomposite formation with metal oxide semiconductors, can enhance its physical, chemical, and electrical properties [23].

In this work, reflux was used for the WO₃ and WO₃/rGO synthesis, at water boiling point and atmospheric pressure. The experiments were carried out at different reaction times for the evaluation of the time effect on the oxide and nanocomposite formation, structural, morphological, and optical properties.

Materials and Methods

The synthesis of WO₃ and WO₃/rGO nanocomposites were carried out by reflux using 3 g of Na₂WO₄·2H₂O as tungsten precursor, 20 ml of hydrochloric acid (HCl), and 0.4 M oxalic acid (H₂C₂O₄) solution [24], at water boiling temperature (100 °C) and atmospheric pressure (1 atm) with constant magnetic stirring. For the preparation of WO₃/rGO nanocomposites were used 0.025 g of GO dispersed in 50 ml of deionized water; GO was synthesized according to [25]. Different experiments were realized during 5, 7.5, and 10 hours to evaluate the reaction time effect on structural and optical properties of WO₃ and WO₃/rGO. After the reaction time the yellow-colored precipitated powders were filtered and washed with deionized water and ethanol. The WO₃ and WO₃/rGO samples were annealing by 5 hours at 500 °C and

350 °C, respectively. The structural characterization of the samples was carried out by X-ray diffraction in a Bruker D8 Advance diffractometer using Cu-K_α radiation ($\lambda = 1.5406 \text{ \AA}$) operated at 40 kV and 40 mA, with a step size of 0.02°. Raman spectra were obtained in a Micro Raman Horiba-Jobin Yvon with a 632.8 nm He-Ne laser. Scanning Electron Microscopy images acquisition was carried out in a JEOL JSM-6610LV microscope at 20 kV and magnification of 15000X. Diffuse reflectance spectra were recorded from compact powders using an UV-Vis Spectrophotometer (Evolution 600).

Results and discussion

The filtered powders of the experiments performed at 5, 7.5, and 10 hours were analyzed by X-ray diffraction (Figure 1). The bottom pattern shows the diffraction peaks of tungsten trioxide hydrate (WO₃(H₂O), tungstite) with orthorhombic structure (PDF 04-011-6930) and tungsten trioxide (WO₃) pure with monoclinic I structure (PDF 04-005-4272); however, with the annealing at 500 °C occur a phase transformation to the monoclinic structure of WO₃ due to dehydration. X-ray diffraction pattern of annealed samples were matched with PDF 04-005-4272 and shows the planes (002), (020), (200), (120), (-112), (022), (202), (-122), (-222), (004), (040), (400), (-114), (420), (340), and (424) located at 23.17°, 23.6°, 24.4°, 26.6°, 28.9°, 33.35°, 34.2°, 35.67°, 41.6, 41.98, 47.35°, 48.3°, 49.9°, 50.7°, 55.8°, 62.35°, and 76.58° respectively; there are no peaks related to another phases. Also, there are no significant changes in peak intensity or position due to reaction time. The lattice parameters obtained at the principal plane are $a = 7.28 \text{ \AA}$, $b = 7.51 \text{ \AA}$, and $c = 7.67 \text{ \AA}$, and d spacing of 3.83 Å [26].

Following the diffractograms of WO₃, the diffraction pattern of rGO is shown with peaks at 12.02°, 26.6°, and 42.5° which correspond to (001), (002), and (101) planes, respectively. The diffractograms of the WO₃/rGO nanocomposites are shown at the top of the graph. The characteristic peak of graphene is not observed in WO₃/rGO nanocomposites because of the low content of rGO and for the reduction of GO to rGO. The WO₃/rGO nanocomposites maintain the crystalline structure of WO₃ in the three different reaction times; however, the ratio of intensities of some WO₃ and WO₃/rGO nanocomposites slightly increased with respect to the increase in reaction time, this agrees with that reported by Jayachandiran *et al.* [27]. Nanocomposites have monoclinic structure, but the diffraction peaks are wide compared with those of the WO₃. In the compounds, the lattice parameters obtained at the principal plane are $a = 7.30$, $b = 7.50$, $c = 7.69 \text{ \AA}$, and d spacing of 3.84 Å. The decrease in the periodicity of the atomic planes in the WO₃/rGO nanocomposites was observed with the evident decrease in the crystallite size of the samples related to the synthesis time [28]. The growth kinetics of WO₃ and WO₃/rGO can be significantly different. In WO₃, crystallite growth can follow a diffusion growth model, where atom mobility is a limiting factor. In contrast, in the case of WO₃/rGO, the presence of rGO can facilitate electron transfer and atom mobility, which can alter the growth

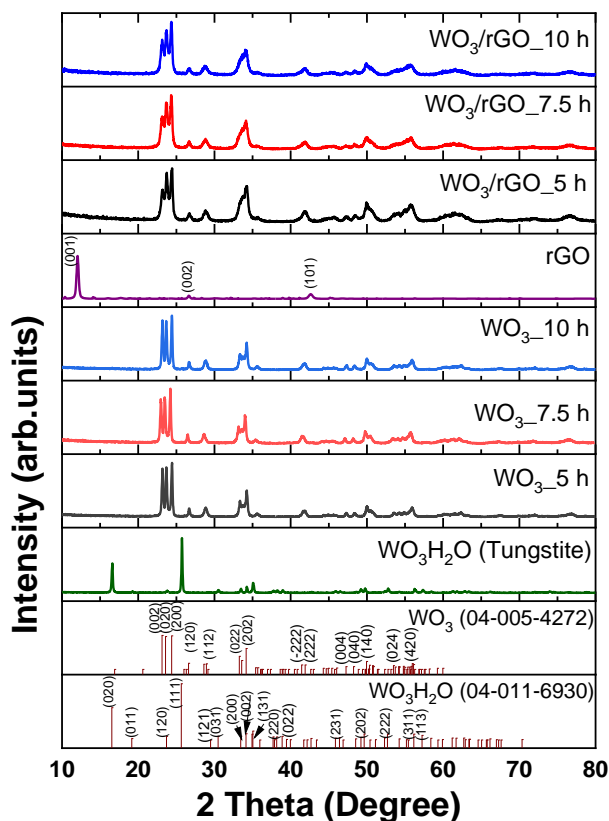


Figure 1. X-ray diffraction patterns of $\text{WO}_3(\text{H}_2\text{O})$, WO_3 and rGO powders. X-ray diffraction patterns of WO_3 and WO_3/rGO obtained at different reaction times (5, 7.5 and 10 hours) and annealed at 500°C for 5 hours.

kinetics. This can result in faster growth or the formation of more complex structures due to the interaction between WO_3 and rGO [29].

The crystallite size of the $\gamma\text{-WO}_3$ and WO_3/rGO obtained at different reaction times was calculated using the Debye-Scherrer's formula [30].

$$D = \frac{0.89\lambda}{\beta \cos\theta}$$

where D is the crystallite size, 0.89 is the Scherrer constant by $\text{Cu-K}\alpha$ radiation in nm, β is the FWHM of diffraction peak and θ the Bragg angle in degrees. The crystallite size calculated for WO_3 obtained at different reaction times was 43.39 nm, 51.06 nm and 51.06 nm, respectively. On the other hand, the crystallite size calculated for WO_3/rGO nanocomposites was 102.14 nm, 58.32 nm, and 40.84 nm obtained at 5, 7.5, and 10 hours, respectively. It is observed that the reaction time in the synthesis of WO_3 and WO_3/rGO significantly affects the crystallinity and morphology. As the reaction time increases, an increase in the crystallinity of WO_3 is observed. This is attributed to the fact that a longer reaction time allows the atoms to organize themselves into a more ordered crystal structure, resulting in a larger crystallite size due to the increase in available thermal energy. In the case of WO_3/rGO , the presence of rGO can influence the nucleation and growth of crystallites, affecting the crystallinity differently compared to pure WO_3 . The interaction between WO_3 and rGO led to the formation of scale-like structures that are distributed over the surface of

rGO, which can be different from the morphology of pure WO_3 , with a monoclinic structure. The growth kinetics for WO_3 and WO_3/rGO differ due to the presence of rGO. While pure WO_3 grows according to its intrinsic chemistry, the inclusion of rGO introduces additional interactions that modify the morphology and can slow down crystallization by competing for ions in solution [29,31].

The interaction between WO_3 and rGO in nanocomposites can be of a chemical and physical nature, depending on the synthesis method used and the specific characteristics of the materials. Available studies indicate that the incorporation of rGO into WO_3 may involve chemical bonds such as C-O-W and C-W bonds, as well as physical interactions such as Van der Waals forces. However, this type of bonds can be determined through the shift of the X-ray diffraction peaks towards lower angles, therefore, based on the XRD characterization performed on the WO_3/rGO nanocomposites, such a shift is not observed, confirming that the interactions between WO_3 and rGO are predominantly physical, manifesting as an anchoring of WO_3 on the rGO surface mediated by Van der Waals forces, contributing to the mechanical stability of the composite [20,29,32].

Raman spectroscopy was used to corroborate the crystalline structure of the obtained samples. Figure 2 shows the A_g phonons of tungstite in 654 cm^{-1} and 949 cm^{-1} , related to stretching mode of W-O and W=O , respectively. Bending or deformation of O-W-O bonds is assigned at 238 cm^{-1} and 433 cm^{-1} , 495 cm^{-1} correspond to C=O bending vibration of remainder oxalic acid ($\delta_{\text{C=O}}$), 710 cm^{-1} and 806 cm^{-1} indication of W-O stretching vibrational modes in WO_6 octahedral units of monoclinic WO_3 [32,33].

For the WO_3 with monoclinic structure, the space group is $\text{P}2_1/\text{n}$ (C_{2h}^5), where there are eight formula units per unit cell; at the Brillouin zone center its normal modes are $\Gamma_{\text{opt}} = 24A_g + 24B_g + 23A_u + 22B_u$, but only de $24A_g$ and $24B_g$ mode are active; therefore, $\Gamma(\text{Raman}) = 24A_g + 24B_g$ [34,35]. In Figure 3, the Raman spectra show the fundamental bands of $\gamma\text{-WO}_3$, at 273.5 and 329.3 cm^{-1} the vibrational modes of O-W-O

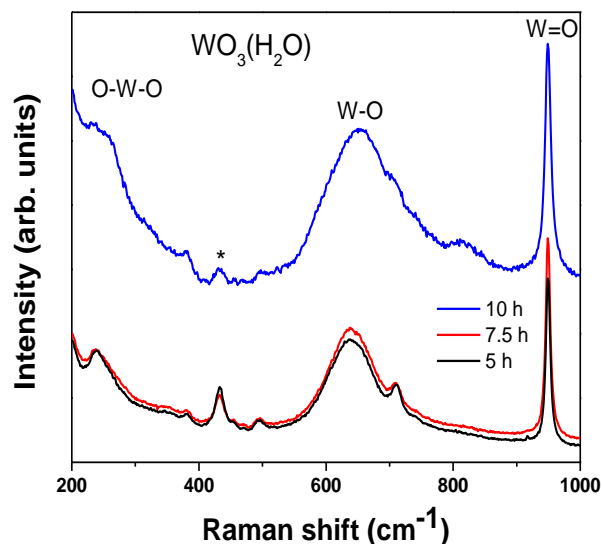


Figure 2. Raman spectra of tungstite samples before thermal treatment.

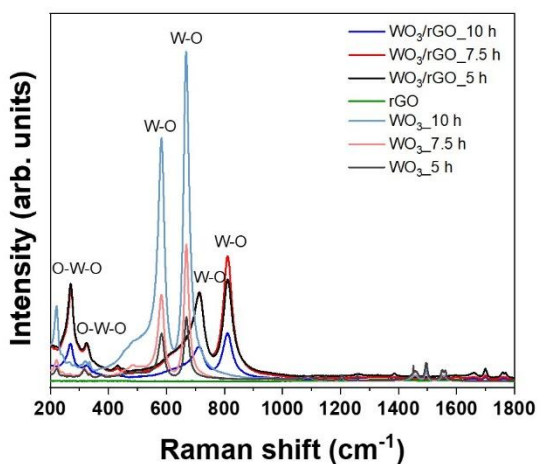


Figure 3. Raman spectra of the WO_3 and WO_3/rGO obtained at different reaction times.

(bending) of the bridging oxygen, and at 718.2 and 809.6 cm^{-1} , the vibrational modes corresponding to W–O (stretching) in WO_6 octahedral units. Additional bands at around 420 and 450 cm^{-1} are characteristic of crystalline tungsten oxides and the shoulder at 612 cm^{-1} could be assigned to O–W–O stretching vibration modes of the bridging oxygen from residual tungstate which decreases in intensity with the temperature rise [36–38].

The Raman spectra of the WO_3/rGO nanocomposites are too shown in Figure 3. Are observed the bands corresponding to $\gamma\text{-WO}_3$ located at 270 and 324 cm^{-1} of O–W–O vibrational modes, the band due to W–O shifted at 713.8 cm^{-1} . The bands at around 430 and 450 cm^{-1} and the shoulder at 612 cm^{-1} are present too. For the WO_3/rGO nanocomposites, there is no evident change in the band location, suggesting that the structure of WO_3 was maintained after the coupling of rGO sheets. The D and G bands in the nanocomposites are slightly shifted as are the bands characteristic of WO_3 , this is attributed to the interaction generated between the oxygens of WO_3 and the carbons of the rGO [39].

In the case of WO_3 , stretching and bending frequencies associated with the O–W–O and W–O bonds are observed. The incorporation of rGO can cause changes in the intensity and position of these vibrational bands. It has been reported that the incorporation of rGO can cause a broadening of the W–O stretching bands, suggesting interactions between the functional groups of rGO and the WO_3 structure. However, no new peaks are observed in the spectra, indicating that the interaction between rGO and WO_3 is a physical interaction. This is because rGO has a two-dimensional structure that allows Van der Waals-type interactions with the WO_3 nanoparticles. These interactions are important for the stability of the nanocomposite and for the uniform dispersion of WO_3 on the rGO surface [21,29].

In the Figure 4, it observed the diamondoid (D) and graphite (G) peaks related to C–C bonds with sp^3 and sp^2 hybridization in GO sample located at 1336.3 and 1599 cm^{-1} , respectively, with the nanocomposite formation, these peaks shifted to 1386 cm^{-1} and 1600 cm^{-1} [32,40]. The

intensity ratio between the D band and the G band is 1.20, 1.24, and 1.25 for the nanocomposites synthesized at 5, 7.5, and 10 h, respectively. This confirms that, synthesizing for 10 h, a greater reduction of GO to rGO is obtained [27].

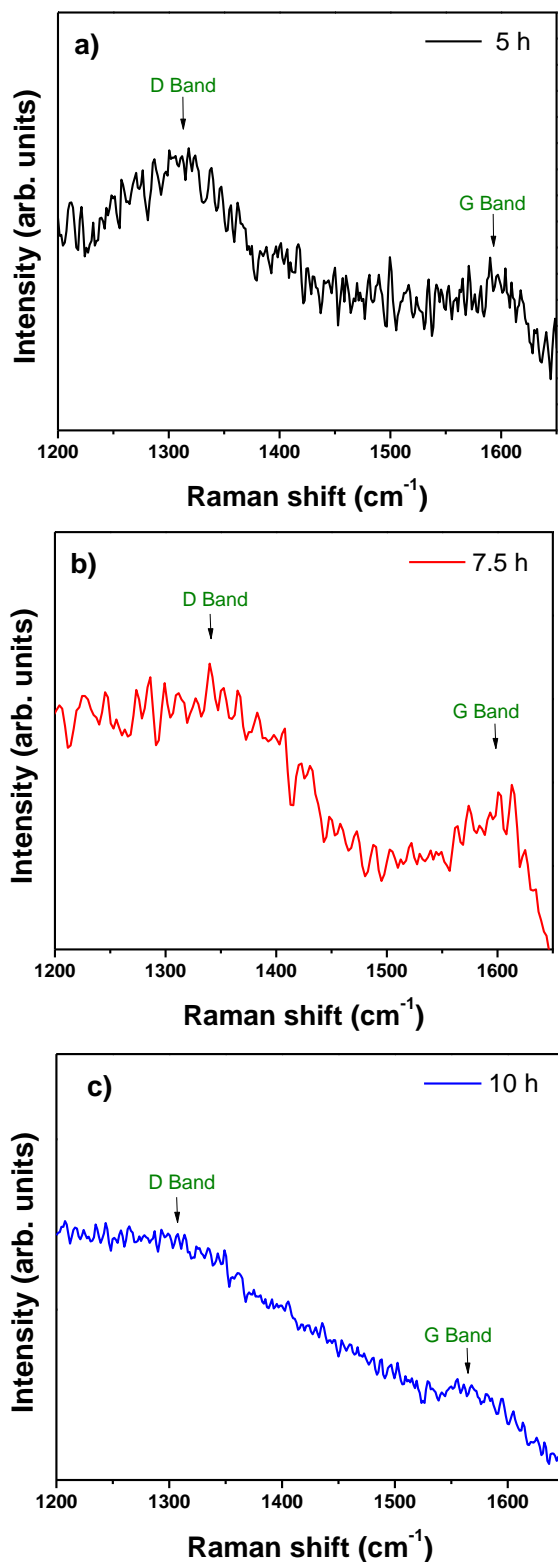


Figure 4. Raman spectra of WO_3/rGO nanocomposites obtained at a) 5 h, b) 7.5 h and c) 10 h in the range of D and G bands of rGO.

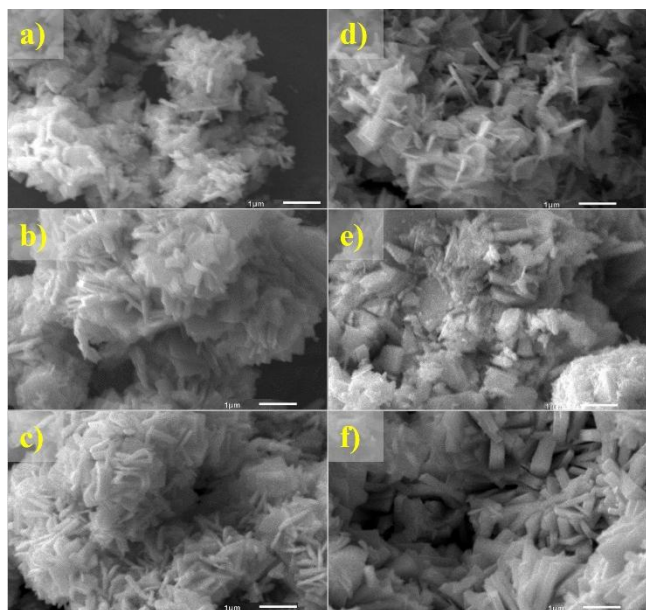


Figure 5. Scanning electron microscopy images of WO_3 nanoplates with rectangular transversal section obtained at a) 5 h, b) 7.5 h, c) 10 h, and WO_3/rGO obtained at d) 5 h, e) 7.5 h f) 10 h.

Scanning electron microscopy images of WO_3 obtained at different reflux times are shown in Figure 5 a) 5 h, b) 7.5 h, and c) 10 h, and the morphology of WO_3/rGO nanocomposites in Figure 5 d) 5 h, e) 7.5 h and f) 10 h. In all figures, it shows that the WO_3 presents a nanoplates structure [41]. It is observed that the nanoplate structure of WO_3 was

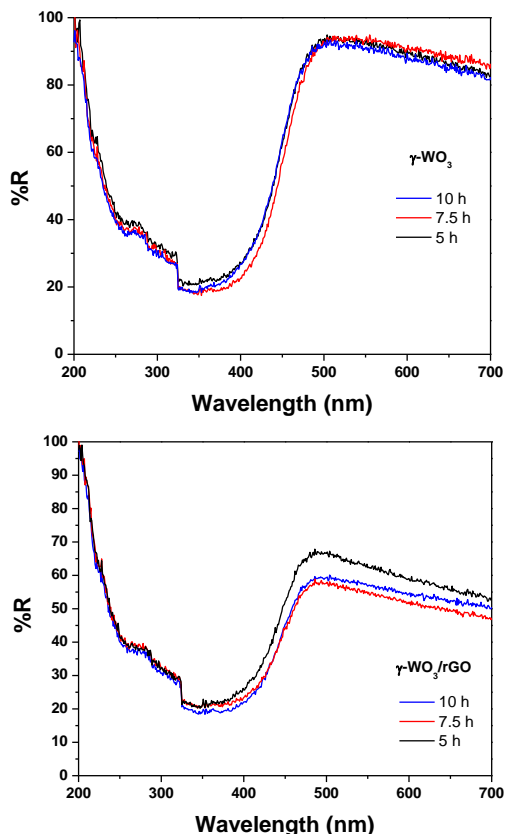


Figure 6. UV-Vis DRS spectra of a) WO_3 and b) WO_3/rGO nanocomposites.

further defined with the addition of rGO. Likewise, the influence of the synthesis time on the arrangement of the nanoplates is observed, where, with a longer synthesis time, the increase in size was evident. The WO_3 particles are randomly oriented in the compounds. In both cases, it is observed that nanoplates rectangular shapes of the WO_3 defined by increasing the synthesis time.

The ultraviolet-visible diffuse reflectance spectra of WO_3 and WO_3/rGO nanocomposites recorded from 200 to 700 nm are shown in Figure 6 (a and b), respectively. In the case of the WO_3 samples, the reflectance percentage is 94% for all

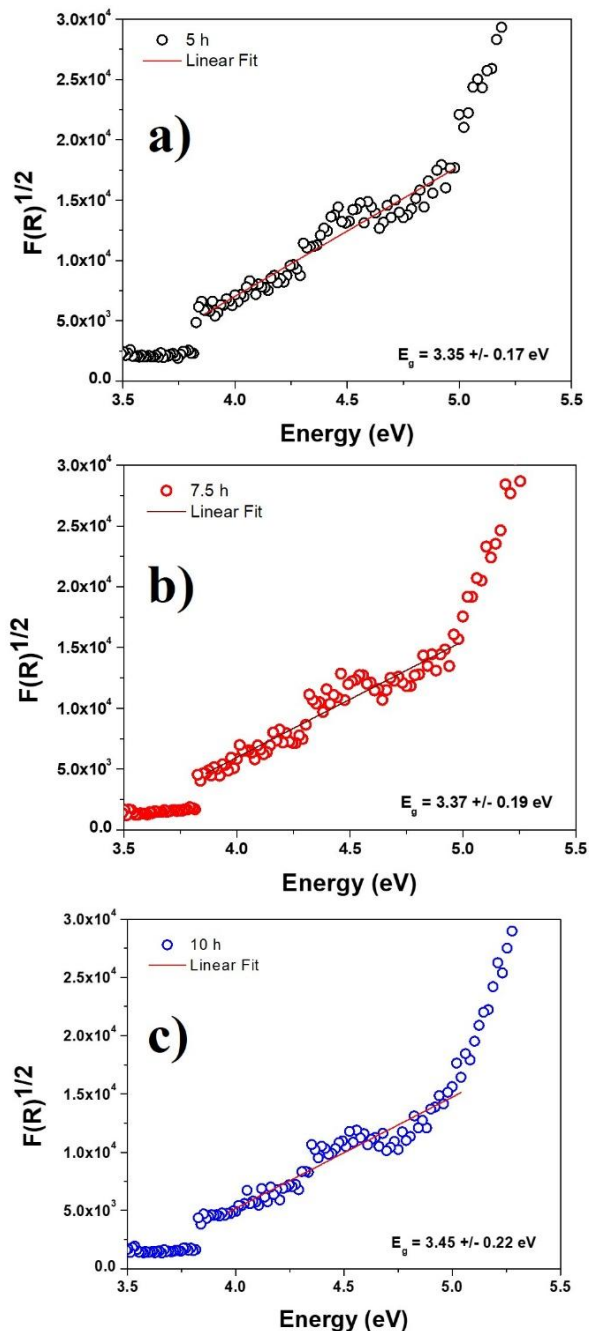


Figure 7. Graphs obtained from the Kubelka-Munk method for the WO_3 samples. The linear range considered for the linear fitting by the Tauc method is between 3.5 and 5.5 eV.

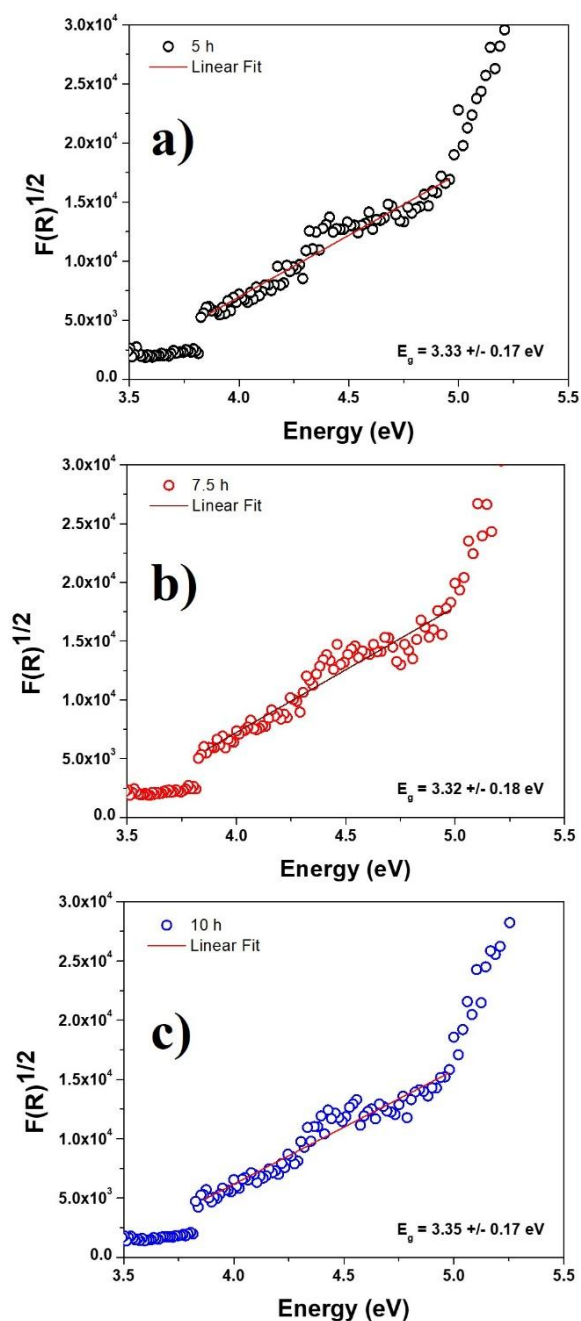


Figure 8. Plots obtained from Kubelka-Munk method for WO_3/rGO nanocomposites. The linear range considered for the linear fitting by the Tauc method is between 3.5 and 5.5 eV.

samples. On the other hand, in WO_3/rGO nanocomposites, the reflectance ranges between 56 and 68%, being in the nanocomposite obtained at 5 hours where the reflectance is greater, derived from a greater dispersion of the incident light [42]. At approximately 325 nm, a change in the spectrum pattern is observed because of the lamp change performed by the equipment. Therefore, the wavelength range of interest is 350 to 700 nm, since the absorption edge of the samples is observed in this range.

Figure 7 shows the band gap (E_g) values obtained from Kubelka-Munk method in a plot of $(F(R))^{1/2}$ vs $E(\text{eV})$ for

indirect transition and extrapolating the slope to $\alpha = 0$, following the Tauc method [43]. The band gap of WO_3 samples synthesized at 5, 7.5 and 10 hours, are a) 3.35 eV, b) 3.37 eV and c) 3.46 eV, respectively.

On the other hand, Figure 8 shows the graphs obtained by the Kubelka-Munk method for WO_3/rGO nanocomposites synthesized at 5, 7.5, and 10 h of reaction. The band gap values obtained through this method are a) 3.33 eV, b) 3.32 eV, and c) 3.35 eV, respectively. After the addition of rGO, a decrease in the band gap value was observed [44].

After the incorporation of rGO into WO_3 , the band gap of the WO_3/rGO nanocomposites showed a slight decrease in the band gap presenting values between 3.32 and 3.35 eV, while the band gap of pure WO_3 is approximately 3.35 to 3.46 eV. This is attributed to the fact that rGO promotes the formation of defects related to oxygen vacancies in WO_3 by increasing the charge carriers in the material. rGO, by acting as an electron acceptor, can modify the Fermi energy level of WO_3 due to its electronic characteristics. In WO_3/rGO nanocomposites, the presence of rGO can introduce defect states into the electronic structure of WO_3 resulting from the interaction between the functional groups on the rGO surface (such as $-\text{COOH}$ and $-\text{OH}$) and the tungsten atoms of WO_3 , creating a favorable environment for charge transfer by providing conductive paths due to its conjugated network of π orbitals, which interact with the electronic states of WO_3 , decreasing the energy required for electronic transitions. These states introduce intermediate energy levels within the WO_3 band gap, acting as bridges between the valence and conduction orbitals of the material facilitating electron transfer between both materials. These interactions improve the photocatalytic activity and electrochemical sensitivity by increasing the efficient generation and separation of electron-hole pairs. This modification can improve the stability of the material and its electrical conductivity, increasing its ability to withstand charge-discharge cycles in optoelectronic applications which can be beneficial for various applications such as sensors and electronic devices [19,29,45,46].

According to the characterizations carried out, including X-ray diffraction (XRD), Raman spectroscopy and Scanning Electron Microscopy (SEM), the synthesis method of the WO_3/rGO nanocomposites by the reflux method is considered reproducible because the results were consistent in terms of the crystalline structure and morphology of the materials obtained. The quality of the reagents used in the synthesis, such as $\text{Na}_2\text{WO}_4 \cdot 2\text{H}_2\text{O}$ and oxalic acid, also plays a fundamental role, since impurities or variations in their purity can affect the result. In addition, the standardized preparation of reduced graphene oxide (rGO) and its adequate dispersion in the reaction medium are essential to ensure that the properties of rGO are consistent in each nanocomposite. Through XRD analysis, it was confirmed that the incorporation of rGO did not alter the monoclinic phase of WO_3 , while Raman spectra showed the presence of the D and G bands of rGO, indicating a uniform formation of the nanocomposite. In addition, SEM micrographs revealed the obtaining of well-defined WO_3 nanoplates in

each synthesis, suggesting that the process can be successfully replicated, thus guaranteeing the reliability and consistency of the synthesis method for future applications.

The absence of secondary phases in the X-ray diffractograms and the consistent results in the morphological and optical properties suggest adequate control of the synthesis parameters, which ensures the reproducibility of the method to obtain high quality materials.

Conclusions

Pure WO₃ and WO₃/rGO nanocomposites were synthesized at different reaction times, 5, 7.5 and 10 hours by the single and low-cost reflux method at 100 °C and 1 atm. The powder products were characterized by structural, morphological, and optical techniques. According to the XRD results, the incorporation of rGO did not cause any change in the crystalline phase of the WO₃ nanostructure. Greater intensity peaks and the increase in the FWHM in the diffractogram of the nanocomposite obtained at 10 h, cause the decrease in the crystallite size with respect to the increase in the synthesis time. Raman spectra confirmed the formation of WO₃/rGO nanocomposites since the D and G bands characteristic of GO were observed. A mostly disordered rGO structure is shown and, consequently, the D band is presented in a higher intensity because of the deformation effects in the sp² hybridization. According to SEM micrographs of the nanocomposites more defined WO₃ nanoplates were obtained at 10 h of reaction. Due to the modification of energy levels of WO₃ by the rGO incorporation, the band gap of the composites decreased with respect to that obtained in pure WO₃, which represents an improvement in the electrical conductivity of the nanocomposites. Through the different characterizations carried out it observed that the WO₃/rGO nanocomposites present better structural, morphological, and electrical properties with respect to pure WO₃, mainly in the nanocomposites synthesized at 10 h; however, the properties of these at 5 and 7.5 h of reaction, present good characteristics for their use in diverse applications.

Acknowledgements

The authors acknowledge to M.T.A. Ana Karen Frias by her technical support in the sample's synthesis. This work was financed by SIP-IPN Multidisciplinary projects 20161804, 20170560 and 20242369. Additionally, the authors thank the following institutions: Laboratorio Central del Instituto de Física "Ing. Luis Rivera Terrazas"– BUAP for the facilities provided for the Micro Raman HORIBA-JOBIN YVON LabRAM-HR, with He-Ne laser of 632.8 nm. Laboratorio GESMAT for the facilities provided for the Raman GemRam BWTek financed by the CONAHCYT Project 2022-321595 and CONAHCYT Ciencia de Frontera 2019-40798. Centro de Investigación en Dispositivos Semiconductores–ICUAP for Diffuse Reflectance measurements. Centro Universitario de Vinculación y Transferencia de Tecnología of Benemérita Universidad

Autónoma de Puebla (CUVyTT-BUAP) for acquisition SEM images and X-ray diffraction measurements.

References

- [1]. C.C. Mardare, A.W. Hassel, *Phys. Status Solidi A* **216**, 1900047 (2019).
- [2]. M.V. Santhosh, K.S. Devaky, M.K. Jayaraj, *Mater. Today: Proc.* **25**, 183 (2020).
- [3]. M. Jamali, F.S. Tehrani, *Mater. Sci. Semicond. Process.* **107**, 104829 (2020).
- [4]. J.D. Muñoz-Bolaños, J.E. Rodríguez-Páez, *Mater. Sci. Eng. B* **274**, 115472 (2021).
- [5]. A. Markhabayeva, *Phys. Sci. Technol.* **10**, 33 (2023).
- [6]. M.T. Goodarzi, M. Ranjbar, *Ceram Int.* **46**, 21248 (2020).
- [7]. L. Ghasemi, H. Jafari, A. Jafari, *J. Aust. Ceram. Soc.* **54**, 483 (2018).
- [8]. K. Mouratis, I.V. Tudose, C. Romanitan, C. Pachiou, M. Popescu, G. Simistiras, S. Couris, M.P. Sucheá, E. Koudoumas, *Coatings* **12**, 545 (2022).
- [9]. W.L. Kwong, N. Savvides, C.C. Sorrell, *Electrochim. Acta* **75**, 371 (2012).
- [10]. N. Bashir, Q.L. Lee, *Mater. Sci. Forum* **1010**, 405 (2020).
- [11]. M. Verma, K.P. Singh, A. Kumar, *Solid State Sci.* **99**, 105847 (2020).
- [12]. S.K. Aditha, A.D. Kurdekar, L.A.A. Chunduri, S. Patnaik, V. Kamiseti, *MethodsX* **3**, 35 (2016).
- [13]. H.S. Nguyen, T.L.A. Luu, H.T. Bui, T.T. Nguyen, H.L. Nguyen, T.S. Nguyen, C.T. Nguyen, *SPMS Conf. Proc.* **2021**, 386 (2022).
- [14]. C. Lee, X. Wei, J.W. Kysar, J. Hone, *Science* **321**, 385 (2008).
- [15]. A. Peigney, Ch. Laurent, E. Flahaut, R.R. Bacsa, A. Rousset, *Carbon* **39**, 507 (2001).
- [16]. A.A. Balandin, S. Ghosh, W. Bao, I. Calizo, D. Teweldebrhan, F. Miao, C.N. Lau, *Nano Lett.* **8**, 902 (2008).
- [17]. A.K. Geim, K.S. Novoselov, *Nature Mater.* **6**, 183 (2007).
- [18]. K.S. Novoselov, A.K. Geim, S.V. Morozov, D. Jiang, Y. Zhang, S.V. Dubonos, I.V. Grigorieva, A.A. Firsov, *Science* **306**, 666 (2004).
- [19]. S.J. Malode, K. Prabhu, S.S. Kalanur, N. Meghani, N.P. Shetti, *Chemosphere* **312**, 137302 (2023).
- [20]. S.J. Malode, K. Prabhu, B.G. Pollet, S.S. Kalanur, N.P. Shetti, *Electrochim. Acta* **429**, 141010 (2022).
- [21]. G. Jeevitha, R. Abhinayaa, D. Mangalaraj, N. Ponpandian, P. Meena, V. Mounasamy, S. Madanagurusamy, *Nanoscale Adv.* **1**, 1799 (2019).
- [22]. A. Eftekhari, H. Garcia, *Mater. Today Chem.* **4**, 1 (2017).
- [23]. S. Rao, J. Upadhyay, K. Polychronopoulou, R. Umer, R. Das, *J. Compos. Sci.* **2**, 25 (2018).
- [24]. H. Hajishafiee, P. Sangpour, N.S. Tabrizi, *Nano* **10**, 1550072 (2015).
- [25]. J. Guerrero-Contreras, F. Caballero-Briones, *Mater. Chem. Phys.* **153**, 209 (2015).
- [26]. M. Ahmadi, S. Sahoo, R. Younesi, A.P.S. Gaur, R.S. Katiyar, M.J-F Guinel, *J. Mater. Sci.* **49**, 5899 (2014).
- [27]. J. Jayachandiran, M. Arivanandhan, O. Padmaraj, R. Jayavel, D. Nedumaran, *Adv. Compos. Hybrid Mater.* **3**, 16 (2020).
- [28]. Y. Waseda, E. Matsubara, K. Shinoda, *X-Ray Diffraction Crystallography* (Springer, Berlin, 2011).
- [29]. S. Bhattacharjee, S. Sen, S. Samanta, S. Kundu, *Electrochim. Acta* **427**, 140820 (2022).
- [30]. E.S. Ameh, *Int. J. Adv. Manuf. Technol.* **105**, 3289 (2019).
- [31]. S. Bandi, A.K. Srivastav, *J. Mater. Sci.* **56**, 6615 (2021).
- [32]. M. Zhi, W. Huang, Q. Shi, M. Wang, Q. Wang, *RSC Adv.* **6**, 67488 (2016).

- [33]. G.M. Hingangavkar, S.A. Kadam, Y.R. Ma, S.D. Sartale, R.N. Mulik, V.B. Patil, *Nano-Struct. Nano-Objects* **34**, 100964 (2023).
- [34]. E. Cazzanelli, C. Vinegoni, G. Mariotto, A. Kuzmin, J. Purans, *Solid State Ion.* **123**, 67 (1999).
- [35]. M. Boulova, N. Rosman, P. Bouvier, G. Lucazeau, *J. Phys.: Condens. Matter* **14**, 5849 (2002).
- [36]. L. Zhou, Q. Ren, X. Zhou, J. Tang, Z. Chen, C. Yu, *Micropor. Mesopor. Mat.* **109**, 248 (2008).
- [37]. A.G. Souza-Filho, V.N. Freire, J.M. Sasaki, J. Mendes Filho, J.F. Julião, U.U. Gomes, *J. Raman Spectrosc.* **31**, 451 (2000).
- [38]. C. Santato, M. Odziemkowski, M. Ulmann, J. Augustynski, *J. Am. Chem. Soc.* **123**, 10639 (2001).
- [39]. J. Kaur, K. Anand, K. Anand, R.C. Singh, *J. Mater. Sci.* **53**, 12894 (2018).
- [40]. K. Ramesh, B. Gnanavel, *Mater. Today Proc.* **47**, 1967 (2021).
- [41]. J. Xiao, C. Song, W. Dong, C. Li, Y. Yin, *Rare Metal Mat. Eng.* **46**, 1241 (2017).
- [42]. A.K. Carranza Díaz, *Espectroscopía de reflectancia difusa - NIR para la determinación del contenido de agua en el suelo*, Master's Thesis (Universidad Nacional de Colombia, 2019).
- [43]. R. López, R. Gómez, *J. Sol-gel Sci. Techn.* **61**, 1 (2012).
- [44]. M. Shur, *Solid-State Electron.* **155**, 65 (2019).
- [45]. B. Parasuraman, S. Chinnapaiyan, B. Kandasamy, P. Shanmugam, A.A. Alothman, P. Thangavelu, C.-H. Huang, *Sens. Actuators A: Phys.* **379**, 115873 (2024).
- [46]. C. Fu, C. Foo, P.S. Lee, *Electrochim. Acta* **117**, 139 (2014).

© 2025 by the authors; licensee SMCTSM, Mexico. This article is an open access article distributed under the terms and conditions of the Creative Commons Attribution license (<http://creativecommons.org/licenses/by/4.0/>).